Received: 23 May 2023 | Revised: 17 August 2023 | Accepted: 18 August 2023

DOI: 10.1002/psc.3540

RESEARCH ARTICLE

Journal of PeptideScience WILEY

Interhelical E@*g*-N@*a* interactions modulate coiled coil stability within a de novo set of orthogonal peptide heterodimers

Anthony R. Perez | Yumie Lee | Michael E. Colvin | Andrea D. Merg

Department of Chemistry and Biochemistry, University of California, Merced, Merced, CA, USA

Correspondence
Andrea D. Merg, Department of Chemistry and Biochemistry, University of California, Merced, 5200 N. Lake Rd., Merced, CA 95343, USA.
Email: amerg@ucmerced.edu

Funding information
NSF, Grant/Award Number: NSF-MRI-2019144; NSF-CREST: Center for Cellular and Biomolecular Machines, Grant/Award Numbers: NSF-HRD-1547848, NSF-HRD-2112675; University of California Office of the President; California Student Aid Commission

The designability of orthogonal coiled coil (CC) dimers, which draw on well-established design rules, plays a pivotal role in fueling the development of CCs as synthetically versatile assembly-directing motifs for the fabrication of bionanomaterials. Here, we aim to expand the synthetic CC toolkit through establishing a "minimalistic" set of orthogonal, de novo CC peptides that comprise 3.5 heptads in length and a single buried Asn to prescribe dimer formation. The designed sequences display excellent partner fidelity, confirmed via circular dichroism (CD) spectroscopy and Ni-NTA binding assays, and are corroborated in silico using molecular dynamics (MD) simulation. Detailed analysis of the MD conformational data highlights the importance of interhelical E@*g*-N@*a* interactions in coordinating an extensive 6-residue hydrogen bonding network that "locks" the interchain Asn-Asn′ contact in place. The enhanced stability imparted to the Asn-Asn′ bond elicits an increase in thermal stability of CCs up to ∼15°C and accounts for significant differences in stability within the collection of similarly designed orthogonal CC pairs. The presented work underlines the utility of MD simulation as a tool for constructing de novo, orthogonal CCs, and presents an alternative handle for modulating the stability of orthogonal CCs via tuning the number of interhelical E@*g*-N@*a* contacts. Expansion of CC design rules is a key ingredient for guiding the design and assembly of more complex, intricate CC-based architectures for tackling a variety of challenges within the fields of nanomedicine and bionanotechnology.

KEYWORDS
coiled coil, de novo peptide design, heterodimers, peptide sequence engineering, self-assembly

1 | INTRODUCTION

As the selected machinery in biology, proteins serve an expansive array of functional roles. Among their many roles, natural proteins mediate a host of chemical transformations, regulate intercellular communications, neutralize pathogens, and serve as integral structural components in connective tissue and the extracellular matrix. The broad utility of proteins undergirds several research fields including protein design, bioengineering, and protein self-assembly, which all aim to broaden and enhance the application scope of proteins for tackling a variety of technological challenges. While naturally occurring proteins represent a logical starting point for the development of protein-based technology, peptides have emerged as viable alternatives for replicating the structure and function of proteins.[1,2] Peptides exhibit the same chemical diversity as proteins and retain many of their structural features including various secondary structures and folding motifs (e.g., alpha helices, collagen triple helices, and coiled coils [CCs]). The short length of peptides facilitates the ability to

establish sequence-to-structure relationships, which can be challenging to elucidate for more complex protein systems. Remarkably, these short amino acid chains still fulfill many of the roles inherent to proteins, including their biological function and assembly (e.g., short RGD peptides facilitate integrin binding).[2,3] Moreover, as synthetically tractable biopolymers, peptides, from a synthetic standpoint, are extremely versatile in that an array of non-proteinogenic motifs can be programmed into the sequence design to create peptide-hybrid molecules via inclusion of non-canonical/peptidomimetic residues (e.g., β-amino acids, peptoids, and aza-glycine),[4–8] oligonucleotides,[9–11] and small molecules.[12] As the repertoire of peptide-based chemical transformations expand, the chemical, structural, and functional scope of peptides will continue to broaden, positioning these biomolecules as key components in the development of novel biomaterials with properties and function that extend beyond nature's capability.

CC peptides and polypeptides have emerged as programmable, biosynthetic tectons for the rational design and construction of artificial protein-mimetic systems and architectures.[13–25] CCs, which consists of two or more alpha helices that intertwine to form a left-handed superhelical coil, are characterized by a seven-residue heptad repeat that is alphabetically assigned *abcdefg* (Figure 1). The driving force for association stems from so called "knobs-into-holes" interactions of hydrophobic side chains of residues that comprise the *a* and *d* positions, which constitute the interhelical interface (Figure 1).[26] Complementary charged residues, which typically occupy the *e* and *g* positions, provide additional stability via interhelical salt bridges and assist in defining the helical orientation (parallel vs. antiparallel).[27]

A key feature of CCs is the ability to direct predetermined pairings between CC peptides through rational engineering of the peptide sequence. Decades of research on CCs have yielded a rich set of design rules and considerations,[28–42] which have allowed for the construction of several collections of orthogonal CC sets.[17,43–53] The well-established sequence-to-structure relationship of CCs distinguishes CC-based assemblies from other peptide self-assembly platforms that rely on relatively non-specific and non-programmable interactions. While current working design rules have brought forth inspirational nanoarchitectures, including de novo protein polyhedral cages,[13] the expansion of CC design rules remains a critical step towards increasing the complexity and function of these architectures for potential applications in nanomedicine and nanobiotechnology.[13,22,46,54–56]

Here, we establish a "minimalistic" set of short, orthogonal CC peptides and employ molecular dynamics (MD) simulations to help provide structural explanations for the experimental binding data. We aimed for a CC set that (1) consists of the minimum length required for forming stable CCs with melting temperature (T_m) values between 30°C and 60°C (an intermediate range that is suitable for dynamic interactions); (2) displays high partner fidelity; and (3) is amenable to analysis by MD simulation to help design potential derivative sequences for incorporation into the CC set. On the basis of these criteria, we settled on a particular de novo sequence design that was first reported by Thomas et al.[32] The parent sequence, which comprises ~3.5 heptads (24 residues), exhibits intermediate stability (T_m = 45°C; K_d = 5.15 ± 2.05 nM) and, importantly, exclusively forms parallel heterodimers. Both features are attributed to the inclusion of a buried polar interaction through placement of Asn in the *a* position. To increase specificity between our designed on-target pairings, a single pair of Asn residues is incorporated at homologous sites only between sequences of designed pairs. This strategy was similarly employed by Plaper et al., in which they utilized a single Asn contact to direct specific parallel dimers between CC peptides comprising 4 heptads.[53] Lastly, we highlight the utility of employing MD simulation to suggest possible binding pairs prior to experimental testing and as a tool to provide a plausible structural rationale of experimentally observed interactions that can be used to generate hypotheses to guide the design of future CC-mediated architectures.

2 | MATERIALS AND METHODS

All chemical reagents were purchased from Sigma-Aldrich Chemical Co. (St. Louis, MO) or Thermo Fisher Scientific Inc. (Waltham, MA) unless otherwise stated. Fmoc amino acids and Rink amide resin were purchased from CEM (Matthews, NC). UV–vis spectra were collected using a Thermo Scientific Nanodrop One UV–vis spectrophotometer. Matrix-assisted laser desorption ionization time-of-flight (MALDI-TOF) mass spectrometry data were collected using a Bruker

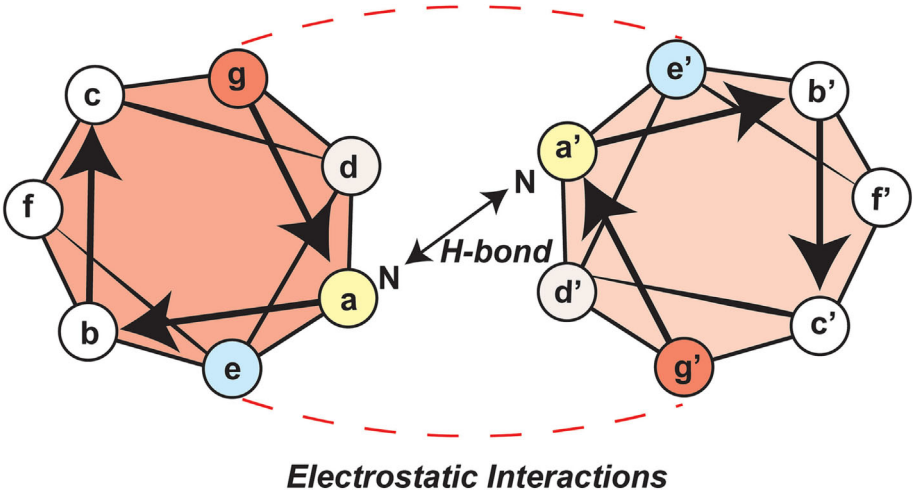

FIGURE 1 Helical wheel diagram for parallel coiled coil (CC) heterodimers showing the N@*a*-N@*a*′ hydrogen bonding interaction and interhelical salt bridges between *g* and *e* positions.

Microflex LRF mass spectrometer (positive reflector mode) and using α-cyano-4-hydroxycinnamic acid (CHCA) as the ionization matrix (1:1 sample to matrix ratio). Liquid chromatography mass spectrometry (LCMS) experiments were conducted using a Q-Exactive Hybrid Quadrupole-Orbitrap mass spectrometer, coupled with a Vanquish UHPLC system (Thermo Scientific, Waltham, MA).

2.1 | Peptide synthesis and purification

Peptides were prepared using microwave-assisted solid-phase peptide synthesis (SPPS) on a CEM Liberty Blue solid-phase peptide synthesizer and ProTide Rink amide resin (CEM). Fmoc-deprotection was achieved with 4-methylpiperidine (20% v/v) in dimethylformamide (DMF). Coupling of amino acids was achieved via *N*,*N*′-diisopropylcarbodiimide/Oxyma pure-mediated activation protocols. Peptides were N-terminally acetylated and C-terminally amidated. After synthesis, the peptidyl resins were filtered, rinsed with acetone, and air-dried. The crude peptides were cleaved from the resin for 3 h at room temperature with a 92.5% trifluoroacetic acid (TFA), 2.5% H_2O, 2.5% 3,6-dioxa-1,8-octanedithiol, 2.5% triisopropylsilane cleavage solution, precipitated with cold diethyl ether, and centrifuged at 4000 rpm for 10 min at 4°C. After centrifugation, the supernatants were discarded, and the pellets were dried under vacuum overnight. Crude peptides were purified by high-performance liquid chromatography (HPLC) using an Agilent 1260 Infinity II HPLC instrument equipped with a preparative scale Phenomenex Kinetex XB-C_{18} column (250 × 30 mm, 5 µm, 100 Å). Peptides were eluted with a linear gradient of acetonitrile-water with 0.1% TFA. The target fractions were collected, rotovaped, and lyophilized. Lyophilized peptides were reconstituted in water and quantified by the UV absorbance at 280 nm using 1280 M^{-1} cm^{-1} as the molar extinction coefficient of tyrosine. Following quantification, each peptide was aliquoted, lyophilized, and stored at −20°C.

2.2 | Circular dichroism (CD)

CD measurements were collected on a Jasco J-1500 spectropolarimeter using a 1-mm path length cuvette (Starna Cells, Inc., Atascadero, CA). Three spectra were recorded and averaged from 260 to 190 nm at a scanning rate of 100 nm/min and a bandwidth of 2 nm. CD thermal denaturation experiments were performed by heating from 5°C to 80°C or 90°C at a rate of 40°C/h. The intensity of the CD signal at 220 nm was recorded as a function of temperature. Lyophilized peptides were reconstituted in 1× phosphate buffered saline (PBS) (pH 7.4), heated to 90°C for 10 min, and cooled (0.5°C/min) to 5°C. Samples were stored at 5°C prior to CD analysis. The helical content was calculated, according to previous methods,[57,58] by converting the ellipticity at 222 nm to mean residue ellipticity (MRE, deg cm^2 dmol·res^{-1}) according to Equation (1):

$$MRE_{222} = \frac{100 \times \theta_{222}}{cnl}, \tag{1}$$

where θ_{222} is the observed signal at 222 nm in mdeg, c is the peptide concentration in mM, n is the number of residues, and l is the path-length of the cuvette. The percent helicity was determined by applying Equations (2)–(5):

$$\%\ helicity = \frac{MRE_{222} - \theta_o}{\theta_{max} - \theta_o}, \tag{2}$$

$$\theta_{max} = \theta_\infty\left(\frac{n-x}{n}\right), \tag{3}$$

$$\theta_\infty = -44000 + 250T, \tag{4}$$

$$\theta_o = 2220 - 53T, \tag{5}$$

where θ_{max} is the maximum MRE for a helix with n number of residues and x is the number of residues assumed to not be helical (in our case $x = 4$). θ_∞ is defined as the theoretical helicity of an infinitely long α-helix that is temperature dependent and was calculated at 5°C. θ_o is defined as the minimum MRE at 222 nm for a random coil at temperature T (in our case $T = 5$°C).

2.3 | Thermodynamic parameters

Thermodynamic parameters were obtained using the method described by Thomas et al. and Marky and Breslauer.[32,59] They were determined by obtaining full CD spectra at 5°C intervals from 5°C to 80°C (16 data points). The sample holder was heated at a 1°C/min heating rate, and the samples were equilibrated for 2 min before full spectra were recorded for 200-, 100-, 50-, 20-, and 2-µM total peptide concentration samples. The spectra were baseline corrected, and the intensity at 222 nm was collected from the spectra and plotted as a function of temperature. The points were fit to a Boltzmann curve using Origin. These experiments were done in triplicate, where the melting temperatures were converted to Kelvin, inverted, and averaged. The averages were plotted against the natural logarithm of the total peptide concentration in molarity with the standard deviation used as the y-error bar. Linear-regression was done in Origin to obtain the slope and the y-intercept that were used to calculate ΔH and ΔS. For non-self-complementary sequences with a molecularity of 2 ($K_{eq} = 4/C_T$), the best-fit line has the form:

$$\frac{1}{T_m} = \frac{R}{\Delta H}\ln C_T + \frac{\Delta S - R\ln 4}{\Delta H} \tag{6}$$

The uncertainties of the slope and y-intercept were used to calculate the uncertainty in K_d by applying the error propagation formula (7).

$$F(x,y); \sigma_F = \sqrt{\frac{\partial F^2}{\partial x}\,\sigma_x{}^2 + \frac{\partial F^2}{\partial x}\,\sigma_y{}^2} \tag{7}$$

2.4 | Size-exclusion chromatography (SEC)

SEC experiments were conducted at 5°C with a 500-µL sample loop on an ÄKTA fast protein liquid chromatography (FPLC) system,

equipped with a Superdex 75 GL 10/300 column. Approximately 500 μL of sample was injected and eluted with 1× PBS (pH 7.4) at a set rate of 0.5 mL/min, and the progress of the separation was monitored at 280 nm. Samples were prepared according to the same protocol used for conducting CD experiments.

2.5 | Ni-NTA binding assay

Three His-tagged variants (His_6-**A**, His_6-**B**, and His_6-**C**), which contain N-terminal GGHHHHHH motifs for binding onto Ni-NTA resin, were synthesized according to the protocol described above. His_6-**A**, His_6-**B**, and His_6-**C** were mixed with equimolar amounts of their on-target partner sequence (**A**′, **B**′, and **C**′, respectively) along with equimolar amounts of the remaining 5 off-target variants (total peptide concentration = 100 μM). Each of these initial solutions was analyzed by LCMS (initial). To three 1.5 mL centrifuge tubes was added 0.5 mL of fresh Ni-NTA slurry (Qiagen Inc.). The slurries were centrifuged for 30 s using a bench top centrifuge followed by removal of the supernatant (20% ethanol). The slurries were then washed three times with 1mL of PBS buffer (pH 7.4) prior to addition of 1 mL of the mixed peptide solutions. After 1 h of gentle mixing on a nutating rocker, the tubes were centrifuged for 30 s, and the supernatants were collected and analyzed via LCMS (supernatant). The resins were spin-washed three times with PBS buffer (pH 7.4), and the bound species were released with 1 mL of 250 mM imidazole in PBS (pH 8.0). After 1 h, the samples were spun down, and the supernatants were analyzed by LCMS (eluent).

2.6 | Molecular dynamic simulations

MD simulations were performed using GROMACS version 2022.3.[60] After short equilibration runs, three replicate 100 ns of MD simulations were run for each structure using the NPT ensemble, the Verlet cutoff scheme, and a 2 fs timestep. All bonds to hydrogen were constrained to their equilibrium length using the LINCS algorithm.[61] Temperature was maintained at 300 K using the Bussi et al thermostat[62] and pressure at 1 bar using the Parrinello-Rahman barostat.[63] The simulations were performed using the AMBER99SB-ILDN force field for the protein[64] and the TIP3P water model.[65] The total system charge was neutralized by Na^+ and Cl^- ions, and additional ions were added to yield a total ion concentration of 70 mM. The root-mean-square structure deviations (RMSDs), root-mean-square fluctuations (RMSFs), number of hydrogen bonds, and number of salt bridges were determined using the GROMACS built-in analysis tools. Average values between 25 and 100 ns were obtained using Origin and the statistics gadget on the plotted figure. For each trajectory, snapshots were taken every nanosecond, and a custom script using the Selenium package (https://www.selenium.dev/) was used to upload each snapshot to the "Protein interfaces, surfaces and assemblies" service (PDBePISA) at the European Bioinformatics Institute (https://www.ebi.ac.uk/pdbe/pisa/).[66]

3 | RESULTS AND DISCUSSION

Three de novo CC pairings (**AA**′, **BB**′, and **CC**′) were designed from six peptide sequences (**A**, **A**′, **B**, **B**′, **C**, and **C**′; Table 1). The sequence architecture follows previous de novo design rules for forming parallel CC dimers in which β-branched, hydrophobic residues (Ile and Leu) populate the *a* and *d* positions, respectively, and complementary charged residues (Glu and Lys) are placed at the *e* and *g* positions to reinforce partner fidelity via introducing attractive and repulsive electrostatic interactions.[38] Alanine, a strong alpha helix promoter,[67,68] comprises the *b* and *c* positions, and various residues (Glu, Lys, Gln, and Tyr) are incorporated at remaining *f* sites and assist in solubility, ease of purification via HPLC, and quantification via UV–vis spectroscopy. An exception is the placement of Asn at a single *a* site. Although this diminishes the stability of CCs, due to disruption of the interhelical hydrophobic interface, the loss in stability is compensated by the increase in specificity for parallel CC dimers via interchain hydrogen bonding.[30,41,44] The Asn residue is strategically placed in different heptads between designed CC pairs to increase the energy gap between on-target and off-target heterodimers.[44] Based on these sequences, the thermodynamically favorable CC fold will (1) have the greatest number of interhelical salt bridges; (2) maximize hydrophobic contact at the interface; and (3) align Asn residues across the helix interface to accommodate enthalpically favorable hydrogen bonds. The partner sequences to **A**, **B**, and **C**, (**A**′, **B**′, and **C**′, respectively) are designed to maximize these enthalpic contributions and contribute to the greatest decrease in the folding free energy. The peptides were synthesized using standard microwave-assisted SPPS and purified via HPLC (Figure S1). The compositions of the peptides were confirmed via MALDI-TOF mass spectrometry (Figure S2).

CD spectroscopy was employed to characterize the folding of each individual peptide (**A**, **B**, **C**, **A**′, **B**′, and **C**′) and the three on-target pairings (**AA**′, **BB**′, and **CC**′; Figure 2). Prior to CD analysis, all peptides (100 μM) were dissolved in PBS (pH 7.4), heated to 90°C, and cooled to 5°C. CD spectra of the individual peptides display varying degrees of alpha helicity as evidenced by differences in the intensity of the CD signal at 208 and 222 nm (Figure 2A–C, Table S1). In all cases, the CD spectra of solutions containing a 1:1 equimolar mixture of the designed on-target peptide pairings exhibit a significant increase in the alpha helical CD signature and, importantly, differ from CD plots corresponding to the sum of the spectra of the individual peptides (Figure 2A–C). Moreover, an increase in the ratio of $\theta_{222}/\theta_{208}$ to values above 1.0 (a range around 1.0 or greater serves as a proxy for the predominance of CC species)[69–71] is observed when both on-target partners are present in solution, with the exception of the C-series in which **C** and **C**′ are relatively structured (Figure 2A–C, Table S1). To assess the fidelity of the on-target dimers, CD spectra for all off-target pairings were collected (Figure S3, Table S1). CD spectra of the mixed peptide solutions closely match with the sum of the individual peptides, which implies a minimal degree of interaction between off-target peptide pairs.

CD thermal denaturation studies were conducted to probe the thermal stability of the CC set, including between off-target pairs

TABLE 1 Sequences of de novo peptides that form orthogonal parallel CC heterodimers.

		def	gabcdef	gabcdef	gabcdef		*a* pattern	*g*/*e* pattern
A	G	LKQ	EIAALEK	ENAALKY	KIAALKQ	G	INI	E (E/K)K
A′	G	LEQ	KIAALKY	ENAALKK	EIAALEQ	G	INI	K (E/K)E
B	G	LKQ	KNAALEY	KIAALKE	KIAALKQ	G	NII	(K/E)KK
B′	G	LEQ	KNAALEK	EIAALEK	EIAALEY	G	NII	(K/E)EE
C	G	LKQ	EIAALKQ	KIAALKY	ENAALKQ	G	IIN	(E/K)K (E/K)
C′	G	LEQ	EIAALKY	EIAALEK	ENAALKQ	G	IIN	(E/K)E (E/K)
B_{EE}	G	LKQ	ENAALEY	KIAALKE	KIAALKQ	G	NII	EKK
B'_{KK}	G	LEQ	KNAALKK	EIAALEK	EIAALEY	G	NII	KEE
B_{EK}	G	LKQ	ENAALKY	KIAALKE	KIAALKQ	G	NII	(E/K)KK
B'_{EK}	G	LEQ	ENAALKK	EIAALEK	EIAALEY	G	NII	(E/K)EE

Abbreviation: CC, coiled coil.

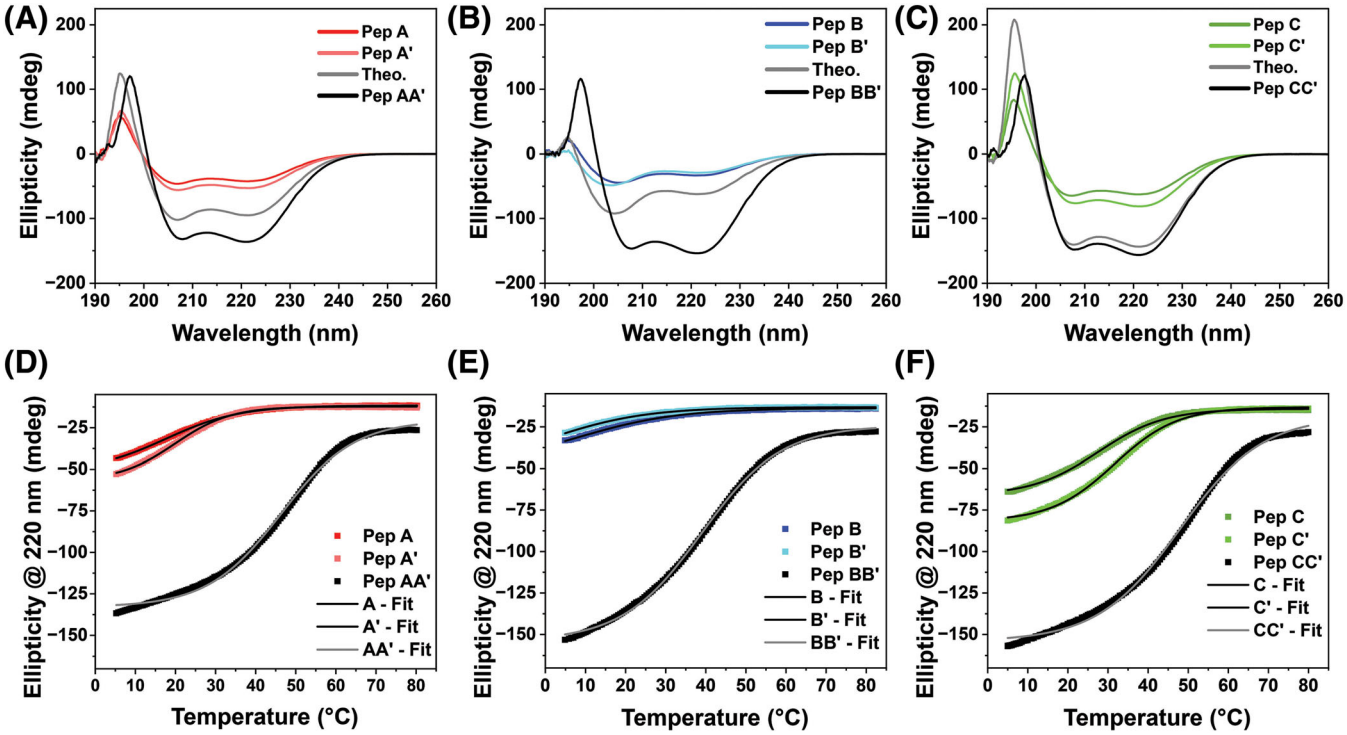

FIGURE 2 Circular dichroism (CD) spectra and thermal denaturation plots for (A) **A**, **A**′, and **AA**′, (B) **B**, **B**′, and **BB**′, and (C) **C**, **C**′, and **CC**′. *Note*: The line labeled "Theo." represents the sum of the plots of the individual peptides. CD thermal melting curves for (D) **A**, **A**′, and **AA**′, (E) **B**, **B**′, and **BB**', and (F) **C**, **C**′, and **CC**′.

(Figure 2D–F). T_m values for the individual peptides, which were only marginally helical, as assessed from CD, vary from <5°C (**B**′) to 32°C (**C**′). The wide range of T_m values for sequences with nearly identical amino acid compositions underlines the notable role that sequence architecture (e.g., distribution of charges) has on the folding propensity. In contrast, T_m values are comparatively higher when complementary designed peptides are mixed in solution ($T_m = 46$°C, 39°C, and 48°C for **AA**′, **BB**′, and **CC**′, respectively; Figure 2D–F). The designed heterodimers all exhibit higher thermal stabilities than the off-target pairings (Figure S4, Table S1). Altogether, the CD data suggest the orthogonality of the de novo CC set. We note, however, from SEC, that solutions containing the on- and off-target peptides elute at similar retention volumes, which precludes the ability to distinguish between monomeric and dimeric species and the presence of non-specific interactions (Figure S5). Such non-specific interactions may explain the relatively high T_m and $\theta_{222}/\theta_{208}$ value of **C** and **C**′ and their off-target variants.

Thermodynamic parameters, obtained from measuring T_m dependence as a function of peptide concentration, confirm the order of thermodynamic stability (**BB**′ < **AA**′ < **CC**), as evidenced by the calculated ΔG values and dissociation constants (K_d; Table 2, Figure S6, Table S2). K_d values of the on-target designs are higher than that of

TABLE 2 Calculated T_m, ΔH, ΔS, ΔG, and K_d values from CD thermal unfolding curves.

	T_m (°C)	ΔH (kJ/mol)	ΔS (J/K·mol)	ΔG (kJ/mol)	Rel ΔG (kJ/mol)	K_d (nM)
AA′	46.3	−152.70	−394.65	−37.01	1.20	254.65 ± 0.41
BB′	38.9	−176.28	−485.59	−33.93	4.27	899.03 ± 1.48
CC′	47.9	−164.72	−431.58	−38.21	0.00	156.42 ± 0.06
$\mathbf{B_{EE}B'_{KK}}$	45.4	−170.40	−453.68	−37.41	0.80	215.86 ± 0.24
$\mathbf{B_{EK}B'_{EK}}$	53.0	−148.07	−370.50	−39.46	−1.25	93.02 ± 0.12

Abbreviation: CD, circular dichroism.

the parent sequence ($K_d \approx 5$ nM).[32] We surmise that the weaker binding interaction of our CC heterodimers stems from the mixed distribution of electrostatic charges along the peptide sequences. The parent sequences are composed solely of Glu or Lys at the *g* and *e* positions, which contrasts the varied electrostatic pattern that we utilized as a means to introduce positive and negative design elements for creating orthogonal parallel pairings. Prior studies have shown that greater intramolecular electrostatic attraction reduces interchain attraction, thereby lowering the thermal stability of CCs.[50] The acquired thermodynamic data foreshadow similarities between **AA′** and **CC′**. Both heterodimers have similar changes in enthalpic and entropic contributions to the free energy of binding, which results in similar K_d values. On the other hand, **BB′** possesses the highest relative free energy primarily due to having the highest entropic penalty of the three on-target designs. This conforms with CD data, which show that **B** and **B′** are least helical (Table S1), and therefore folding between these monomers must pay a high entropic cost. Even with the increased entropic penalty, we report that the K_d value of **BC′**, which represents the off-target mixture that exhibits the highest T_m is still significantly higher than **BB′** (5000 vs. 899 nM; Figure S6).

While CD provides evidence that the specified dimers fold into CCs with greater stability in comparison to solutions containing off-target pairings, additional experiments were conducted to test their orthogonality, that is, the exclusive binding between partner strands in the presence of multiple CC forming peptides, using a Ni-NTA binding assay.[52] His_6-**A**, His_6-**B**, and His_6-**C** (Figure S7), which all contain an N-terminal GlyGly$(His)_6$ tag, were synthesized and mixed with their respective binding partners (**A′**, **B′**, and **C′**) and the remaining off-target sequences in the presence of Ni-NTA resin. LCMS analysis of the initial mixed solution before transfer to Ni-NTA resin ("initial"), the supernatant after exposure to Ni-NTA ("supernatant"), and solution collected after washing with imidazole ("eluent") confirm a high degree of dimer specificity between on-target peptide pairs (Figure 3 and Table S3). In all cases, the target peptides (**A′**, **B′**, and **C′**) and their on-target His-tagged partners (His_6-**A**, His_6-**B**, and His_6-**C**, respectively) were nearly exclusively present in the imidazole-washed solution (Figure 3, "eluent"). These results demonstrate the orthogonality of our CC peptide set. We next assessed the agreement between MD simulations and the experimental data, and potentially elucidate the apparent differences between the three on-target dimers.

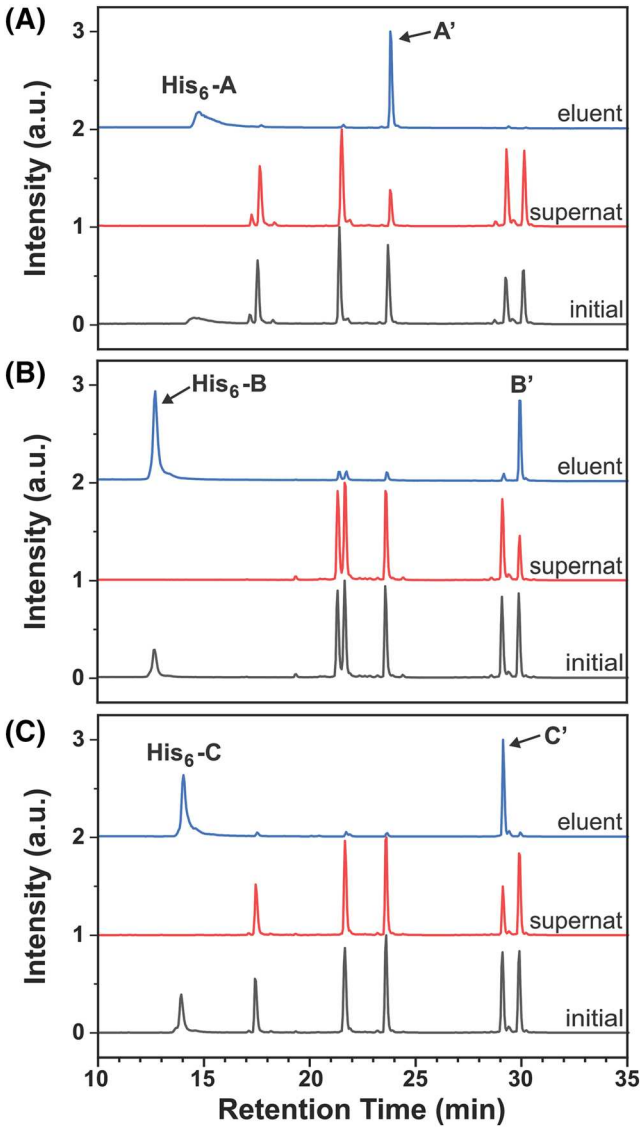

FIGURE 3 Ni-NTA analysis of the "initial" (prior to exposure to Ni-NTA resin), "supernatant" (solution containing unbound peptides after exposure to Ni-NTA resin), and "eluent" (bound peptides released after imidazole wash) samples containing (A) His_6-**A**, (B) His_6-**B**, and (C) His_6-**C** and their on-target peptide partner and the remaining off-target peptides. Liquid chromatography mass spectrometry (LCMS) analysis of each peak is found in Table S3.

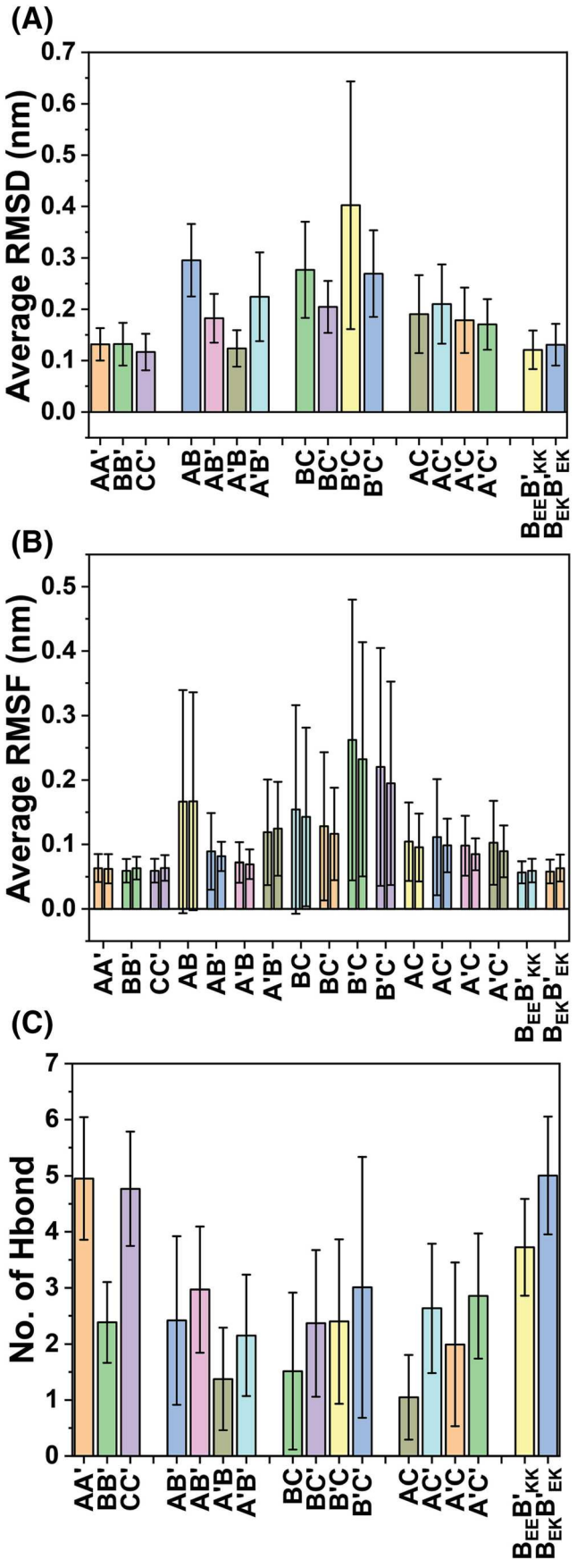

FIGURE 4 Average (A) root-mean-square structure deviation (RMSD), (B) root-mean-square fluctuation (RMSF) (for residues at the *a* and *d* positions), and (C) number of interhelical hydrogen bonds for all 17 simulated pairs. Tabulated values can be found in Table S4.

3.1 | MD simulations resolve differences between on- and off-target dimers

MD simulations were performed on all on-target and off-target heterodimers (15 total pairs). For each pair, 100-ns simulations were carried out at 300 K in triplicate using the GROMACS software package[60] and the AMBER99SB-ILDN force field.[64] Initial structures were constructed from point-mutations in Pymol using the PDB of CC-Di obtained from CCBuilder2.0.[31,72] RMSD, which measures the structural deviation of backbone atoms from starting positions, for on-target pairs (**AA**′, **BB**′, and **CC**′) displays low RMSD values that remain constant throughout the duration of the simulation (Figures 4A and S8). In contrast, off-target complexes, with the exception of **A'B**, were far more dynamic with greater structural deviations and run-to-run variability, implying that these CC dimers are weakly bound (Figure S9). Similarly, the RMSF, which measures the individual mobility of the C_α along the peptide sequence, at the *a* and *d* positions (i.e., residues that constitute the interhelical interface) is comparatively lower for on-target complexes than their off-target counterparts (Figures 4B and S10–S11). Altogether, RMSD and RMSF analyses indicate that the designed CC pairs maintain tight interhelical contacts that persist throughout the CC interface, unlike the off-target dimers that exhibit greater structural fluctuations and mobility (Table S4). These results are consistent with the CD thermal denaturation experiments, in which on-target heterodimers display higher T_m values (greater thermal stability) in comparison with the off-target complexes (Table S1).

While RMSD and RMSF data correctly distinguish (apart from **A'B**) differences in stability *between* the on-target and off-target variants, both sets of data are unable to adequately recapitulate the finer differences in thermal stability *within* the on-target and off-target variants. In some cases, RMSD and RMSF data accurately resolve relative differences in CC stability between off-target designs (e.g., **A'B** and **BC**′ both have the lowest RMSD/RMSF values and highest T_m within their group). However, in many cases, the RMSD and RMSF data on their own fail to resolve the experimental results, including the notable difference in thermal stability between **BB**′ and the other on-target dimers (**AA**′ and **CC**′), and especially when comparing off-target dimers between groups (e.g., T_m of **BC**′ > > T_m of **A'B**). We attribute the discrepancy between MD simulation and CD analysis to the large variability that is observed between triplicate runs, especially for off-target pairings, in which standard deviations overlap across the different samples (Figure 4A,B). The results highlight the suitability of our relatively short timescale MD simulations to predict stability between on-target and off-target dimers and demonstrate its limitation in resolving finer differences between CC dimers that contain few attractive/stable contacts. Alternative MD protocols, at much larger

aggregate computational costs, could potentially be employed to improve correlation between experimental and computational results, such as carrying out simulated annealing and/or employing replica exchange molecular dynamics (REMD) simulation to more completely sample configuration space across multiple temperatures or much longer time scale simulations leading to chain separation or denaturation events.

3.2 | Extensive hydrogen bonding network stabilizes interhelical Asn-Asn′ contact

Notable differences emerge between on-target heterodimers when comparing the average number of hydrogen bonds obtained from the MD simulations (Figure 4C). While **AA**′ and **CC**′ average ~5 interchain hydrogen bonds for the duration of the simulations, which far exceeds the off-target heterodimers, **BB**′ possesses on average only ~2.5 hydrogen bonds (on par with the off-target pairs; Figures 4C and S12–S13). Unlike RMSD and RMSF, in which **BB**′ exhibits similar values to **AA**′ and **CC**′ (Figure 4A,B), the decreased number of interhelical hydrogen bonds observed for **BB**′ provided the first possible insight for explaining the comparatively lower T_m and higher K_d value of **BB**′. This distinct result for **BB**′ was further confirmed by analysis of the number of interchain salt bridges, in which **BB**′ exhibits fewer salt bridges, on average (0.63 for **BB**′ vs. 1.03 and 0.89 for **AA**′ and **CC**′, respectively; Figures S14–S16).

In-depth investigation via PDBePISA analysis, which provides detailed information regarding interchain surface contacts including hydrogen bonds and salt bridges, reveals key differences that distinguish **BB**′ from the other designed heterodimers. Although the Asn-Asn′ hydrogen bond represents the interhelical contact with the highest percentage of occurrence for all three on-target pairs, the percentage of time during the simulations that this hydrogen bond was present is, on average, lower for **BB**′ (79%) compared with **AA**′ and **CC**′ (98% and 99%, respectively; Figure S17A, Table S5). Additionally, the two interhelical E@*g*-N@*a* contacts (E@*g*′-N@*a*/E@*g*-N@*a*′) that surround the Asn-Asn′ bond are engaged in hydrogen bonding for 64%/85% and 89%/66% of the simulation time for **AA**′ and **CC**′ (Figure S17B,C and Table S6). This long-lived interaction is absent for **BB**′ as Lys precedes Asn for **B** and **B**′ (Table 1). The presence of interhelical E@*g*-N@*a* hydrogen bonds corroborate a previous report by Hodges and coworkers, which disclosed the stabilizing effect of this particular interaction within the crystal structure of cortexillin I/GCN4 hybrid CC peptides.[42] They revealed that E@*g*-N@*a* interactions form a network of hydrogen bonds that stabilize the Asn-Asn′ core region of the dimer.

Snapshots of the MD simulations for **AA**′ and **CC**′ reveal a slightly modified version of the previously reported hydrogen bonding network.[42] In our case, using MD simulations, we observe a more extended hydrogen bonding network that connects across the *g*-*a*′-*a*-*g*′ layer (Glu-Asn′-Asn-Glu′; Figure 5). Within this network, peripheral E@*g* and E@*g*′ residues, which flank the interhelical Asn interaction, appear to "lock" the Asn pair in place via hydrogen bonds. Additionally, MD trajectories show that Lys at *e* and *e*′ readily form interchain salt bridges with the flanking Glu residues to create a more expansive hydrogen bonding network that spans across 6 residues (Lys′-Glu-Asn′-Asn-Glu′-Lys) and explains the increase in the number of salt bridges, on average, for **AA**′ and **CC**′ (Figure S16). The asymmetric engagement of E@*g*-N@*a*′ and E@*g*′-N@*a* interactions is attributed to the added stability associated with an intrahelical Lys-Asn hydrogen bond that can only form on one side of the CC interface (Figure 5A).[42] From PDBePISA analysis, the prevalence of Glu-Lys contacts is markedly higher within the heptad that contains the Asn-Asn′ contact (Figure S17D and Table S7), indicating that the Glu-Asn′-Asn-Glu′ hydrogen bonding network spatially orients the E@*g*/*g*′ in an ideal configuration that is predisposed for forming interhelical salt bridges (Figure 5A). The presence of Lys at the *g* and *g*′ sites prevents the organization of this extended hydrogen bonding network for **BB**′. In this case, the alignment of side-chain carbonyl groups of Asn in one direction, which are co-planar when engaged, inhibits one carbonyl from accepting hydrogens from the side-chain amine of Lys (Figure 5A). Furthermore, the extended length of K@*g*/*g*′ cannot accommodate both salt bridge formation (with Glu located across the helix) and a hydrogen bond with Asn.

The increase in stability afforded by the hydrogen bonding network present within **AA**′ and **CC**′ is substantiated through analysis of the bond distance and conformational dynamics of the Asn-Asn′ interaction. Shorter Asn-Asn′ bond distances of **AA**′ and **CC**′ (1.92 ± 0.15 and 1.92 ± 0.14 Å, respectively) compared with **BB**′ (2.00 ± 0.49 Å) corroborate the tighter packing and hence increased stability of the former pairs (Figure S18).[45] Previous studies have shown that the buried Asn side chains are highly dynamic, exchanging between three primary configurations that are based on whether the side-chain is directed towards the interface ("inside," $\chi1 \approx -60°$, *gauche*), away from the interface ("out," $\chi1 \approx +60°$, *gauche*$^-$), or somewhere in-between ("middle," $\chi1 \approx \pm180°$, *trans*).[33] Side-chain dihedral angles of all three on-target dimers consist of the preferred "inside-middle" (or identical "middle-inside") arrangement ($\chi1 \approx -70°$ and $\chi1 \approx \pm180°$), which accommodates the hydrogen bonding between the interhelical Asn residues (Figure S19). However, although the dihedral angles remain unchanged for all three on-target pairs, a flip from "inside-middle" to "middle-inside" was only observed within the second simulation run for **BB**′ (Figure S19B,E). While using much longer simulation times and/or employing alternative MD techniques with enhanced conformational sampling (e.g., REMD) would be required to fully map the conformational space of interchain Asn interactions, at a significantly increased computational cost, our results support the hypothesis that the decreased thermostability of **BB**′ is attributed to the weaker and more dynamic interchain Asn-Asn' contact.

In summary, interhelical E@*g*-N@*a* hydrogen bonds, which have been previously reported,[42] are responsible for coordinating a hydrogen bonding network that stabilizes the CC interface by "locking" the Asn-Asn′ contact in place. The presence of this bonding network is further stabilized through long-lived Glu-Lys salt bridges that form almost exclusively between Glu/Lys pairs that are in the immediate proximity to the Asn-Asn′ bond. Replacement of Glu with Lys at the proximal *g* and *g*′ position precludes the formation of this CC-

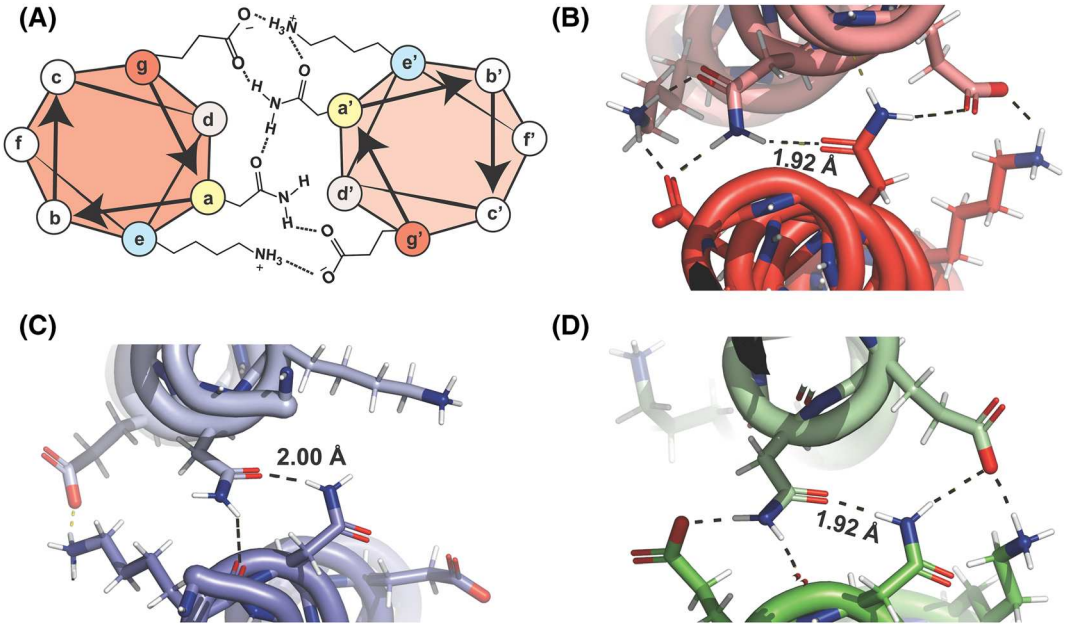

FIGURE 5 (A) Helical wheel diagram depicting the interhelical *g*-*a*′-*a*-*g*′ hydrogen bonding network that is observed when E@*g*-N@*a* contacts are present, including salt bridge contacts between *e* and *g* positions and a single intrahelical K@*e*′-N@*a*′ hydrogen bond. Snapshot of the molecular dynamics (MD) simulations highlighting the hydrogen bonding interactions (dashed lines) that are present in proximity to the interhelical Asn-Asn′ contact for (B) **AA**′, (C) **BB**′, and (D) **CC**′. Average Asn-Asn′ bond distances are also displayed.

stabilizing hydrogen bonding pattern, which leads to a weaker and more dynamic Asn-Asn′ interaction, and ultimately manifests via the lower CC thermostability of **BB**′. Moreover, our results underscore the value of MD simulations as a supplementary tool to both guide the design of new CC dimers and to suggest plausible structural rationales for experimental results. This mutual feedback between model-based design and experimental validation can be leveraged to gain greater clarity in resolving the various competing interactions present within the CC interface.[33]

3.3 | Redesign of BB′ with Glu-Asn interactions increases CC thermostability

We hypothesized that redesigning **BB**′ with Glu preceding Asn should give rise to the hydrogen bonding network present within **AA**′ and **CC**′ and thus enhance the stability of **BB**′. MD simulations were conducted on two redesigned **BB**′ pairs having one ($\mathbf{B_{EE}}$ and $\mathbf{B'_{KK}}$) or two ($\mathbf{B_{EK}}$ and $\mathbf{B'_{EK}}$) Glu residues installed at the *g*/*g*′ positions within the *g*-*a*′-*a*-*g*′ layer comprising the interchain Asn-Asn′ bond (subscripts of the redesigned sequences denote the electrostatic pattern within the Asn-containing heptad; Table 1). If they work as predicted, these new sequence designs will add an exciting new degree of freedom in specifying the stability of heterodimeric CCs as a function of the number of interhelical E@*g*-N@*a* interactions. Our MD simulations of these new structures show that the RMSD and RMSF values are comparable with the original on-target heterodimers (Figures 4A,B and S20A,B, S21A,B), but as hypothesized, the average number of hydrogen bonds for $\mathbf{B_{EE}B'_{KK}}$ and $\mathbf{B_{EK}B'_{EK}}$ is increased step-wise from ~3.7 to ~5.0, respectively, with the latter pairing commensurate with the average number of hydrogen bonds for **AA**′ and **CC**′ (Figures 4C and S20C, S21C). Furthermore, the average Asn-Asn′ bond distance was shortened to 1.94 ± 0.16 and 1.91 ± 0.13 Å for $\mathbf{B_{EE}B'_{KK}}$ and $\mathbf{B_{EK}B'_{EK}}$, respectively, suggesting that $\mathbf{B_{EK}B'_{EK}}$ is potentially more stable than the other on-target dimers (Figures S20F and S21F). PDBePISA analysis reveals that only a single installation of interhelical E@*g*-N@*a* interactions ($\mathbf{B_{EE}B'_{KK}}$) is required to bring the percent occurrence of the Asn-Asn′ contact on par with **AA**′ and **CC**′ (Figure S17A, Table S5). Furthermore, the predominant Glu-Lys salt bridge interaction is restored back to the Glu/Lys pairs that are peripheral to the Asn-Asn′ bond—a significant departure from **BB**′, in which the Glu-Lys contacts are most prevalent at the C-terminus (Figure S17D). Visualization of the MD trajectory for $\mathbf{B_{EK}B'_{EK}}$ confirms the full extension of the hydrogen bonding network (Lys′-Glu-Asn′-Asn-Glu′-Lys) that was present in **AA**′ and **CC**′ but absent in **BB**′ (Figure 6B). As expected, with only a single interhelical E@*g*-N@*a* contact available, only half of the hydrogen bonding network is observed for $\mathbf{B_{EE}B'_{KK}}$ (Figure 6A).

To test these theoretical predictions, the four new **B** variants were synthesized, isolated, and characterized (Table 1, Figures S22 and S23). The predictions from MD simulations of the redesigned sequences were successfully verified experimentally. CD and SEC data of the redesigned dimer species verify that they form dimeric CCs (Figures 6C and S24), and as expected, thermal denaturation of $\mathbf{B_{EE}B'_{KK}}$ and $\mathbf{B_{EK}B'_{EK}}$ reveals a step-wise increase in thermostability (T_m of 45°C and 53°C, respectively; Figures 6D and S25) in comparison with **BB**′ ($T_m = 39$°C; Figure 2E). The T_m observed for $\mathbf{B_{EK}B'_{EK}}$ actually exceeds that of **AA**′ and **CC**′. These results are consistent with prior studies that demonstrated that buried polar Asn-Asn′ interactions

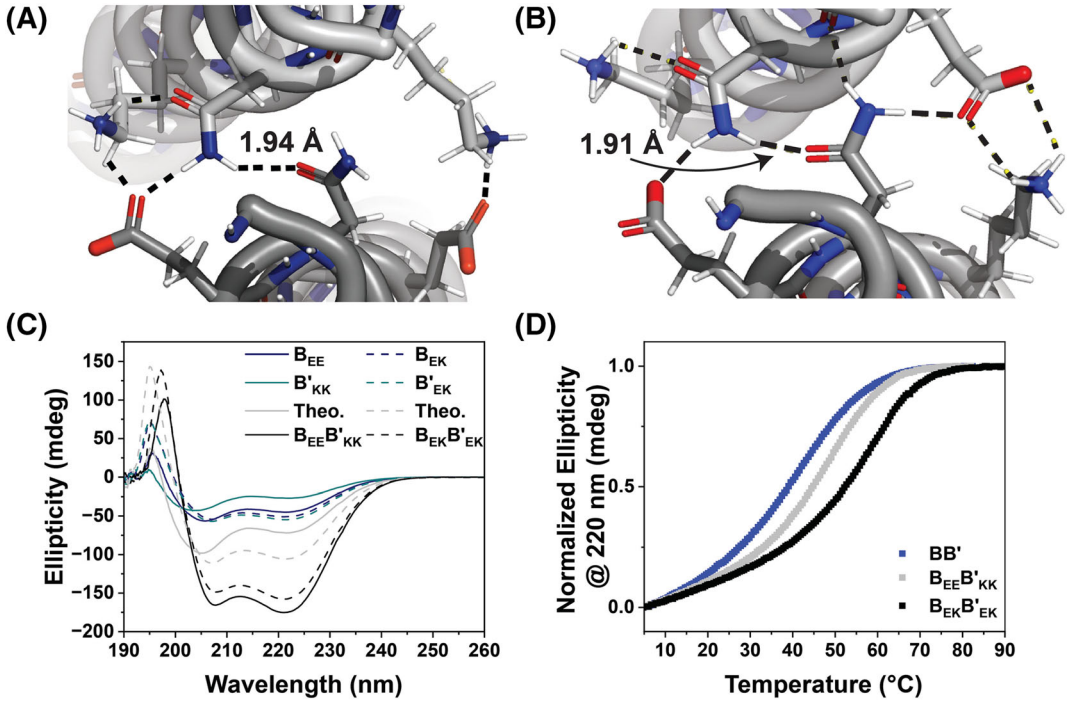

FIGURE 6 Snapshots of the molecular dynamics (MD) simulation of (A) $\mathbf{B_{EE}B'_{KK}}$ and (B) $\mathbf{B_{EK}B'_{EK}}$ revealing the limited and extensive hydrogen bonding network, respectively, around the shortened interchain Asn-Asn′ bond. (C) CD spectra of $\mathbf{B_{EE}}$, $\mathbf{B'_{KK}}$, $\mathbf{B_{EK}}$, $\mathbf{B'_{EK}}$, $\mathbf{B_{EE}B'_{KK}}$, and $\mathbf{B_{EK}B'_{EK}}$. (D) Normalized thermal denaturation profiles of **BB′**, $\mathbf{B_{EE}B'_{KK}}$, and $\mathbf{B_{EK}B'_{EK}}$, which display the increase in T_m as a function of the number of interchain E@*g*-N@*a* contacts present within the dimer.

are less disruptive to the hydrophobic interface when excluded from the core region, and as a result, sequences with Asn incorporated near the termini exhibit greater thermostability.[30] Thermodynamic parameters for $\mathbf{B_{EE}B'_{KK}}$ and $\mathbf{B_{EK}B'_{EK}}$ reveal the step-wise decrease in the free energy as a function of installing either one or two interhelical E@*g*-N@*a* contacts, respectively (Table 2, Figure S26). From this analysis, an individual Glu-Asn contact results in an approximate 3.48 kJ/mol increase in stability, when compared with **BB′**, and two Glu-Asn contacts result in a 5.53 kJ/mol increase in stability. The nonadditive increase may be attributed to the fact that the intrahelical Lys-Asn hydrogen bond can only be present on one side of the helix (see above). These results are consistent with the prior work that reported, on average, a 0.74 kcal/mol (3.1 kJ/mol) increase in stability per interchain E@*g*-N@*a* pair after correcting for changes in helix propensity.[42] We note that, in our case, the increased helical content of the B variants is an additional factor that likely accounts for some degree of stabilization of the CC (Table S8). Lastly, the increased stability results in a 4× and 10× decrease in K_d values for $\mathbf{B_{EE}B'_{KK}}$ and $\mathbf{B_{EK}B'_{EK}}$, respectively (Table 2). Altogether, the results demonstrate that the CC stability within our de novo peptide set can be systematically modulated by controlling the number of interhelical E@*g*-N@*a* interactions.

CONCLUSION

We establish a de novo set of orthogonal CC peptides that comprise 3.5 heptads in length and contains a single buried polar interaction to dictate dimer specificity. CD analysis of the on- and off-target heterodimers and Ni-NTA binding assays confirm the fidelity of the designed on-target pairs and are consistent with results from MD simulations, which identify possible differential interactions between on- and off-target dimers, thus providing a tool to help guide the development of future orthogonal CCs for synthesis and experimental validation. In addition, comprehensive analysis of the MD data uncovers two key design considerations that can be employed for tuning the thermostability and binding strength between similarly designed orthogonal CC sequences. First, interhelical Glu-Asn interactions coordinate a long-range E@*g*-N@*a′*-N@*a*-E@*g′* hydrogen bonding network that stabilizes the CC interface by locking the interhelical Asn-Asn′ contact in place. This leads to a substantial ∼10-fold decrease in K_d (>14°C increase in T_m) when compared with similar CC sequences that do not contain interhelical E@*g*-N@*a* bonds. This design consideration provides an additional handle to modulate the stability of commonly utilized Asn-containing CCs with minimal alterations to the peptide sequence design. Second, Glu-Lys salt bridging contacts, which are available throughout the CC, occur much more frequently for Glu/Lys pairs that immediately flank the Asn-Asn′ bond and contribute to the organization of a more expansive 6-residue hydrogen bonding network (Lys′-Glu-Asn′-Asn-Glu′-Lys) that provides additional stability around the Asn-Asn′ contact. We envision that this second consideration will help direct future orthogonal CC sequence designs by focusing positive and negative design elements within the heptad(s) that comprise(s) Asn, leading to increased energy gap differences between on- and off-target designs. Finally, our results highlight the utility of MD simulation as a

supporting method to experimental studies to develop additional CC sequence design rules that can be incorporated into the CC toolkit and allow for the construction of more complex and dynamic architectures with greater level of control over their properties.

ACKNOWLEDGEMENTS

This work was supported by the University of California, Merced. A.R.P. acknowledges fellowship support from the NSF-CREST: Center for Cellular and Biomolecular Machines at UC Merced (NSF-HRD-1547848 and NSF-HRD-2112675) and UC Merced. Y.L. acknowledges fellowship support from UC LEADS (funded by the University of California Office of the President) and LAEP (funded by the California Student Aid Commission). We acknowledge computing time on the Pinnacles cluster at UC Merced (NSF-MRI-2019144). We thank Prof. Son Nguyen for use of the DLS instrument, Prof. Shahar Sukenik for helpful comments and discussion, and Dr. Mourad Sadqi for LCMS data collection. We also thank Dr. Lauren Stark for access to her PDBePISA driver and analysis scripts and Joseph McTiernan for help with analyzing the MD results.

ORCID

Andrea D. Merg https://orcid.org/0000-0002-2293-5267

REFERENCES

1. Sinha NJ, Langenstein MG, Pochan DJ, Kloxin CJ, Saven JG. Peptide design and self-assembly into targeted nanostructure and functional materials. *Chem Rev*. 2021;121(22):13915-13935. doi:10.1021/acs.chemrev.1c00712
2. Groß A, Hashimoto C, Sticht H, Eichler J. Synthetic peptides as protein mimics. *Front Bioeng Biotechnol*. 2015;3:211. doi:10.3389/fbioe.2015.00211
3. Ruoslahti E. RGD and other recognition sequences for integrins. *Annu Rev Cell Dev Biol*. 1996;12(1):697-715. doi:10.1146/annurev.cellbio.12.1.697
4. Zhang Y, Malamakal RM, Chenoweth DM. Aza-glycine induces collagen hyperstability. *J Am Chem Soc*. 2015;137(39):12422-12425. doi:10.1021/jacs.5b04590
5. Kessler JL, Kang G, Qin Z, et al. Peptoid residues make diverse, hyperstable collagen triple-helices. *J Am Chem Soc*. 2021;143(29):10910-10919. doi:10.1021/jacs.1c00708
6. Goodman M, Melacini G, Feng Y. Collagen-like triple helices incorporating peptoid residues. *J Am Chem Soc*. 1996;118(44):10928-10929. doi:10.1021/ja961717i
7. Hodgson DRW, Sanderson JM. The synthesis of peptides and proteins containing non-natural amino acids. *Chem Soc Rev*. 2004;33(7):422-430. doi:10.1039/b312953p
8. Aguilar M-I, Purcell AW, Devi R, et al. β-Amino acid-containing hybrid peptides—new opportunities in peptidomimetics. *Org Biomol Chem*. 2007;5(18):2884-2890. doi:10.1039/b708507a
9. Stephanopoulos N. Peptide–oligonucleotide hybrid molecules for bioactive nanomaterials. *Bioconjug Chem*. 2019;30:1915-1922. doi:10.1021/acs.bioconjchem.9b00259
10. MacCulloch T, Buchberger A, Stephanopoulos N. Emerging applications of peptide–oligonucleotide conjugates: bioactive scaffolds, self-assembling systems, and hybrid nanomaterials. *Org Biomol Chem*. 2019;17(7):1668-1682. doi:10.1039/C8OB02436G
11. Tung C-H, Stein S. Preparation and applications of peptide−oligonucleotide conjugates. *Bioconjug Chem*. 2000;11(5):605-618. doi:10.1021/bc0000334
12. Wu Y, Williams J, Calder EDD, Walport LJ. Strategies to expand peptide functionality through hybridisation with a small molecule component. *RSC Chem Biol*. 2021;2(1):151-165. doi:10.1039/D0CB00167H
13. Lapenta F, Aupič J, Strmšek Ž, Jerala R. Coiled coil protein origami: from modular design principles towards biotechnological applications. *Chem Soc Rev*. 2018;47(10):3530-3542. doi:10.1039/C7CS00822H
14. Fletcher JM, Harniman RL, Barnes FRH, et al. Self-assembling cages from coiled-coil peptide modules. *Science*. 2013;340(6132):595-599. doi:10.1126/science.1233936
15. Aupič J, Lapenta F, Strmšek Z, Merljak E, Plaper T, Jerala R. Metal ion-regulated assembly of designed modular protein cages. *Sci Adv*. 2022;8(24):eabm8243. doi:10.1126/sciadv.abm8243
16. Ljubetič A, Lapenta F, Gradisar H, et al. Design of coiled-coil protein-origami cages that self-assemble in vitro and in vivo. *Nat Biotechnol*. 2017;35(11):1094-1101. doi:10.1038/nbt.3994
17. Park WM, Bedewy M, Berggren KK, Keating AE. Modular assembly of a protein nanotriangle using orthogonally interacting coiled coils. *Sci Rep*. 2017;7(1):10577. doi:10.1038/s41598-017-10918-6
18. Lapenta F, Aupič J, Vezzoli M, et al. Self-assembly and regulation of protein cages from pre-organised coiled-coil modules. *Nat Commun*. 2021;12(1):939. doi:10.1038/s41467-021-21184-6
19. Boyle AL, Bromley EHC, Bartlett GJ, et al. Squaring the circle in peptide assembly: from fibers to discrete nanostructures by de novo design. *J Am Chem Soc*. 2012;134(37):15457-15467. doi:10.1021/ja3053943
20. Xu C, Liu R, Mehta AK, et al. Rational design of helical nanotubes from self-assembly of coiled-coil lock washers. *J Am Chem Soc*. 2013;135(41):15565-15578. doi:10.1021/ja4074529
21. Pandya MJ, Spooner GM, Sunde M, Thorpe JR, Rodger A, Woolfson DN. Sticky-end assembly of a designed peptide fiber provides insight into protein fibrillogenesis. *Biochemistry*. 2000;39(30):8728-8734. doi:10.1021/bi000246g
22. Jorgensen MD, Chmielewski J. Recent advances in coiled-coil peptide materials and their biomedical applications. *Chem Commun*. 2022;58(83):11625-11636. doi:10.1039/D2CC04434J
23. Nepal M, Sheedlo MJ, Das C, Chmielewski J. Accessing three-dimensional crystals with incorporated guests through metal-directed coiled-coil peptide assembly. *J Am Chem Soc*. 2016;138(34):11051-11057. doi:10.1021/jacs.6b06708
24. Jiang L, Zuo X, Li J, Traaseth NJ, Kirshenbaum K. Programmed supramolecular assemblies using orthogonal pairs of heterodimeric coiled coil peptides. *Angew Chem Int Ed*. 2022;61(27):e202201895. doi:10.1002/anie.202201895
25. Jiang Y, Zhang W, Yang F, et al. Molecular design of stapled pentapeptides as building blocks of self-assembled coiled coil–like fibers. *Sci Adv*. 2021;7:eabd0492. doi:10.1126/sciadv.abd0492
26. Crick F. The packing of [alpha]-helices: simple coiled-coils. *Acta Crystallogr*. 1953;6(8):689-697. doi:10.1107/S0365110X53001964
27. Monera OD, Kay CM, Hodges RS. Electrostatic interactions control the parallel and antiparallel orientation of .alpha.-helical chains in two-stranded .alpha.-helical coiled-coils. *Biochemistry*. 1994;33:3862-3871. doi:10.1021/bi00179a010
28. McClain DL, Woods HL, Oakley MG. Design and characterization of a heterodimeric coiled coil that forms exclusively with an antiparallel relative helix orientation. *J Am Chem Soc*. 2001;123(13):3151-3152. doi:10.1021/ja004099l
29. Oakley MG, Kim PS. A buried polar interaction can direct the relative orientation of helices in a coiled coil. *Biochemistry*. 1998;37(36):12603-12610. doi:10.1021/bi981269m
30. Fletcher JM, Bartlett GJ, Boyle AL, et al. N@a and N@d: oligomer and partner specification by asparagine in coiled-coil interfaces. *ACS Chem Biol*. 2017;12(2):528-538. doi:10.1021/acschembio.6b00935

31. Fletcher JM, Boyle AL, Bruning M, et al. A basis set of de novo coiled-coil peptide oligomers for rational protein design and synthetic biology. *ACS Synth Biol*. 2012;1(6):240-250. doi:10.1021/sb300028q
32. Thomas F, Boyle AL, Burton AJ, Woolfson DN. A set of de novo designed parallel heterodimeric coiled coils with quantified dissociation constants in the micromolar to sub-nanomolar regime. *J Am Chem Soc*. 2013;135(13):5161-5166. doi:10.1021/ja312310g
33. Thomas F, Niitsu A, Oregioni A, Bartlett GJ, Woolfson DN. Conformational dynamics of asparagine at coiled-coil interfaces. *Biochemistry*. 2017;56(50):6544-6554. doi:10.1021/acs.biochem.7b00848
34. Woolfson DN. *Advances in Protein Chemistry*. Vol. 70. Academic Press; 2005:79-112.
35. Mason JM, Arndt KM. Coiled coil domains: stability, specificity, and biological implications. *ChemBioChem*. 2004;5(2):170-176. doi:10.1002/cbic.200300781
36. O'Shea EK, Lumb KJ, Kim PS. Peptide 'Velcro': design of a heterodimeric coiled coil. *Curr Biol*. 1993;3(10):658-667. doi:10.1016/0960-9822(93)90063-T
37. Zhu B-Y, Zhou ME, Kay CM, Hodges RS. Packing and hydrophobicity effects on protein folding and stability: effects of β-branched amino acids, valine and isoleucine, on the formation and stability of two-stranded α-helical coiled coils/leucine zippers. *Protein Sci*. 1993;2(3):383-394. doi:10.1002/pro.5560020310
38. Woolfson DN. In: Parry DAD, Squire JM, eds. *Fibrous Proteins: Structures and Mechanisms*. Springer International Publishing; 2017:35-61.
39. Grigoryan G, Keating AE. Structural specificity in coiled-coil interactions. *Curr Opin Struct Biol*. 2008;18(4):477-483. doi:10.1016/j.sbi.2008.04.008
40. Drobnak I, Gradišar H, Ljubetič A, Merljak E, Jerala R. Modulation of coiled-coil dimer stability through surface residues while preserving pairing specificity. *J Am Chem Soc*. 2017;139(24):8229-8236. doi:10.1021/jacs.7b01690
41. Harbury PB, Zhang T, Kim PS, Alber TA. Switch between two-, three-, and four-stranded coiled coils in GCN4 leucine zipper mutants. *Science*. 1993;262(5138):1401-1407. doi:10.1126/science.8248779
42. Lee DL, Ivaninskii S, Burkhard P, Hodges RS. Unique stabilizing interactions identified in the two-stranded α-helical coiled-coil: crystal structure of a cortexillin I/GCN4 hybrid coiled-coil peptide. *Protein Sci*. 2003;12(7):1395-1405. doi:10.1110/ps.0241403
43. Bromley EHC, Sessions RB, Thomson AR, Woolfson DN. Designed α-helical Tectons for constructing multicomponent synthetic biological systems. *J Am Chem Soc*. 2009;131(3):928-930. doi:10.1021/ja804231a
44. Gradišar H, Jerala R. De novo design of orthogonal peptide pairs forming parallel coiled-coil heterodimers. *J Pept Sci*. 2011;17(2):100-106. doi:10.1002/psc.1331
45. Aronsson C, Danmark S, Zhou F, et al. Self-sorting heterodimeric coiled coil peptides with defined and tuneable self-assembly properties. *Sci Rep*. 2015;5(1):14063. doi:10.1038/srep14063
46. Lebar T, Lainšček D, Merljak E, Aupič J, Jerala R. A tunable orthogonal coiled-coil interaction toolbox for engineering mammalian cells. *Nat Chem Biol*. 2020;16(5):513-519. doi:10.1038/s41589-019-0443-y
47. Daudey GA, Shen M, Singhal A, et al. Liposome fusion with orthogonal coiled coil peptides as fusogens: the efficacy of roleplaying peptides. *Chem Sci*. 2021;12(41):13782-13792. doi:10.1039/D0SC06635D
48. Negron C, Keating AE. A set of computationally designed orthogonal antiparallel homodimers that expands the synthetic coiled-coil toolkit. *J Am Chem Soc*. 136(47):16544-16556. doi:10.1021/ja507847t
49. Crooks RO, Baxter D, Panek AS, Lubben AT, Mason JM. Deriving heterospecific self-assembling protein–protein interactions using a computational Interactome screen. *J Mol Biol*. 2016;428(2 Pt A):385-398. doi:10.1016/j.jmb.2015.11.022
50. Crooks RO, Lathbridge A, Panek AS, Mason JM. Computational prediction and design for creating iteratively larger heterospecific coiled coil sets. *Biochemistry*. 2017;56(11):1573-1584. doi:10.1021/acs.biochem.7b00047
51. Reinke AW, Grant RA, Keating AE. A synthetic coiled-coil interactome provides heterospecific modules for molecular engineering. *J Am Chem Soc*. 2010;132(17):6025-6031. doi:10.1021/ja907617a
52. Diss ML, Kennan AJ. Orthogonal recognition in dimeric coiled coils via buried polar-group modulation. *J Am Chem Soc*. 2008;130(4):1321-1327. doi:10.1021/ja076265w
53. Plaper T, Aupič J, Dekleva P, et al. Coiled-coil heterodimers with increased stability for cellular regulation and sensing SARS-CoV-2 spike protein-mediated cell fusion. *Sci Rep*. 2021;11(1):9136. doi:10.1038/s41598-021-88315-3
54. Kim BJ, Yang D, Xu B. Emerging applications of supramolecular peptide assemblies. *Trends Chem*. 2020;2(1):71-83. doi:10.1016/j.trechm.2019.09.004
55. Levin A, Hakala TA, Schnaider L, Bernardes GJL, Gazit E, Knowles TPJ. Biomimetic peptide self-assembly for functional materials. *Nat Rev Chem*. 2020;4(11):615-634. doi:10.1038/s41570-020-0215-y
56. Morris C, Glennie SJ, Lam HS, et al. A modular vaccine platform combining self-assembled peptide cages and immunogenic peptides. *Adv Funct Mater*. 2019;29(8):1807357. doi:10.1002/adfm.201807357
57. Luo P, Baldwin RL. Mechanism of helix induction by trifluoroethanol: a framework for extrapolating the helix-forming properties of peptides from trifluoroethanol/water mixtures back to water. *Biochemistry*. 1997;36(27):8413-8421. doi:10.1021/bi9707133
58. Crone NSA, Kros A, Boyle AL. Modulation of coiled-coil binding strength and Fusogenicity through peptide stapling. *Bioconjug Chem*. 2020;31(3):834-843. doi:10.1021/acs.bioconjchem.0c00009
59. Marky LA, Breslauer KJ. Calculating thermodynamic data for transitions of any molecularity from equilibrium melting curves. *Biopolymers*. 1987;26(9):1601-1620. doi:10.1002/bip.360260911
60. Abraham MJ, Murtola T, Schulz R, et al. GROMACS: high performance molecular simulations through multi-level parallelism from laptops to supercomputers. *SoftwareX*. 2015;1-2:19-25. doi:10.1016/j.softx.2015.06.001
61. Hess B, Bekker H, Berendsen HJC, Fraaije JGEM. LINCS: a linear constraint solver for molecular simulations. *J Comput Chem*. 1997;18(12):1463-1472. doi:10.1002/(SICI)1096-987X(199709)18:123.0.CO;2-H
62. Bussi G, Donadio D, Parrinello M. Canonical sampling through velocity rescaling. *J Chem Phys*. 2007;126(1):014101. doi:10.1063/1.2408420
63. Parrinello M, Rahman A. Polymorphic transitions in single crystals: a new molecular dynamics method. *J Appl Phys; (United States)*. 1981;52(12):7182-7190. doi:10.1063/1.328693
64. Lindorff-Larsen K, Piana S, Palmo K, et al. Improved side-chain torsion potentials for the Amber ff99SB protein force field. *Proteins: Struct Funct Bioinformatics*. 2010;78(8):1950-1958. doi:10.1002/prot.22711
65. Jorgensen WL, Chandrasekhar J, Madura JD, Impey RW, Klein ML. Comparison of simple potential functions for simulating liquid water. *J Chem Phys*. 1983;79(2):926-935. doi:10.1063/1.445869
66. Krissinel E, Henrick K. Inference of macromolecular assemblies from crystalline state. *J Mol Biol*. 2007;372(3):774-797. doi:10.1016/j.jmb.2007.05.022
67. Lyu PC, Liff MI, Marky LA, Kallenbach NR. Side chain contributions to the stability of alpha-helical structure in peptides. *Science*. 1990;250(4981):669-673. doi:10.1126/science.2237416
68. O'Neil KT, DeGrado WF. A thermodynamic scale for the helix-forming tendencies of the commonly occurring amino acids. *Science*. 1990;250(4981):646-651. doi:10.1126/science.2237415
69. Kiss RS, Weers PMM, Narayanaswami V, Cohen J, Kay CM, Ryan RO. Structure-guided protein engineering modulates helix bundle

exchangeable apolipoprotein properties. *J Biol Chem*. 2003;278(24): 21952-21959. doi:10.1074/jbc.M302676200

70. Crooks RO, Rao T, Mason JM. Truncation, randomization, and selection: generation of a reduced length c-Jun antagonist that retains high interaction stability. *J Biol Chem*. 2011;286(34):29470-29479. doi:10.1074/jbc.M111.221267
71. Jiang L, Kirshenbaum K. A modular approach for organizing dimeric coiled coils on peptoid oligomer scaffolds. *Org Biomol Chem*. 2020; 18(12):2312-2320. doi:10.1039/D0OB00453G
72. Wood CW, Woolfson DN. CCBuilder 2.0: powerful and accessible coiled-coil modeling. *Protein Sci*. 2018;27(1):103-111. doi:10.1002/pro.3279

SUPPORTING INFORMATION

Additional supporting information can be found online in the Supporting Information section at the end of this article.

How to cite this article: Perez AR, Lee Y, Colvin ME, Merg AD. Interhelical E@*g*-N@*a* interactions modulate coiled coil stability within a de novo set of orthogonal peptide heterodimers. *J Pept Sci*. 2023;e3540. doi:10.1002/psc.3540